PHYSICAL REVIEW E **90**, 062202 (2014)

Drag-force regimes in granular impact

Mukesh Tiwari,[1,*] T. R. Krishna Mohan,[2,†] and Surajit Sen[3,‡]
[1]*Dhirubhai Ambani Institute of Information and Communication Technology (DA-IICT), 382007 Gandhinagar, India*
[2]*CSIR Centre for Mathematical Modelling and Computer Simulation (C-MMACS), Bangalore 560017, India*
[3]*Department of Physics, State University of New York, Buffalo, New York 14260-1500, USA*
(Received 1 April 2014; revised manuscript received 27 October 2014; published 1 December 2014)

We study the penetration dynamics of a projectile incident normally on a substrate comprising of smaller granular particles in three-dimensions using the discrete element method. Scaling of the penetration depth is consistent with experimental observations for *small* velocity impacts. Our studies are consistent with the observation that the normal or drag force experienced by the penetrating grain obeys the generalized Poncelet law, which has been extensively invoked in understanding the drag force in the recent experimental data. We find that the normal force experienced by the projectile consists of position and kinetic-energy-dependent pieces. Three different penetration regimes are identified in our studies for low-impact velocities. The first two regimes are observed immediately after the impact and in the early penetration stage, respectively, during which the drag force is seen to depend on the kinetic energy. The depth dependence of the drag force becomes significant in the third regime when the projectile is moving slowly and is partially immersed in the substrate. These regimes relate to the different configurations of the bed: the initial loose surface packed state, fluidized bed below the region of impact, and the state after the crater formation commences.

DOI: 10.1103/PhysRevE.90.062202 PACS number(s): 45.70.−n, 47.57.Gc, 83.80.Fg, 81.70.Bt

I. INTRODUCTION

The problem of energy propagation and dissipation when a high-energy projectile strikes a granular medium is of fundamental importance. Understanding of the channels through which the energy of the projectile is dissipated as it moves through a granular medium will have widespread implications in designing efficient shock absorbers for high-velocity impacts and in understanding the processes associated with the formation of impact craters. During the past decade this loss of energy has been extensively investigated through measurements of penetration depth [1–9], crater morphology [10–12], and evolution of force networks [13,14] in the substrate, and so on. For low-impact energies, it is well established that the final penetration depth scales as one-third the power of the total fall height [1,2,15]. For larger impact energies and denser projectiles a 1/4 power law has also been observed [11].

While the interaction between the projectile and the substrate is rather complex and further investigations are still required for a complete understanding, simple phenomenological models based on experiments and computer simulations have been proposed. The prevalent view and the *unified picture* that has emerged from these studies [2,3,13,16,17] is that the projectile motion after impact can be assumed to follow the generalized Poncelet law,

$$m\ddot{z} = mg - F_n = mg - f(z) - h(z)\dot{z}^2, \qquad (1)$$

where F_n is the total drag or normal force acting on the projectile and consists of two parts. At large velocities, the normal force F_n is dominated by the kinetic energy. At small velocities, the $h(z)\dot{z}^2$ term becomes less important and a depth-dependent behavior characterized by $f(z)$ is seen. mg is the force due to gravity. m and z are the mass and position of the projectile respectively. $z = 0$ is associated with the location of the upper unperturbed surface of the bed. The exact nature of these resistive forces depend on the system parameters, geometry of the projectile, and impact regime and are contained within the terms $f(z)$ and $h(z)$.

$h(z)$ is usually assumed to be a constant, whereas different forms for $f(z)$ have been suggested. In Ref. [17] it is argued that the depth dependence of the drag force for shallow impact varies as the square of the depth and is a constant for deep impact. Notably, the square dependence on depth, without the velocity dependence of the drag force in Eq. (1), naturally leads to the one-third scaling of penetration depth [17]. In Ref. [2] an exponential depth-dependent drag force which goes from quadratic at low penetration depth to a constant at large depths was obtained from fits to experimental data. However, a frictional drag force which varies linearly with depth has also been observed [2,16,18,19].

In this paper we present results of 3D impact simulations with particular attention devoted to the validity of Eq. (1). The paper is laid out as follows. Details of the numerical simulations are presented in Sec. II. In Sec. III we present results for the scaling of the penetration depth for a large range of impact velocities. We compare our results for the force experienced by the projectile with Eq. (1), which enables us to get further insight into the penetration dynamics. Conclusions are presented at the end.

II. NUMERICAL METHOD

We study the impact dynamics of the projectile by performing three dimensional discrete element method (DEM) simulations. The numerical simulations have been performed using the open-source DEM software YADE [20]. The target granular bed is first prepared by creating a loose random packing of spheres in a rectangular container surrounded by hard walls. The sides of the container are of length 30 cm and

*mukesh_tiwari@daiict.ac.in
†kmohan@cmmacs.ernet.in
‡sen@buffalo.edu

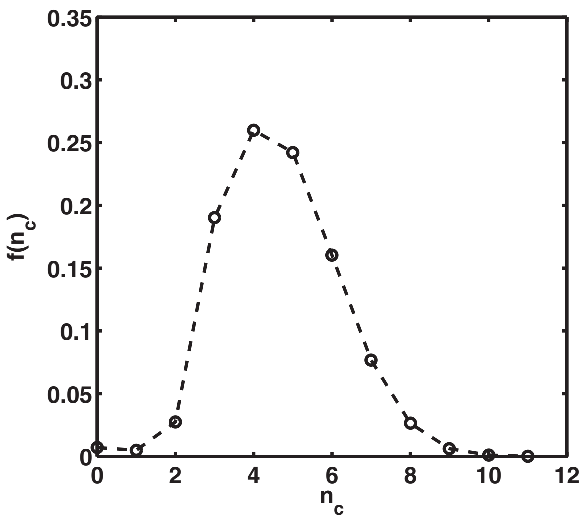

FIG. 1. Distribution of coordination number for the granular bed. $f(n_c)$ is the fraction of particles with n_c contacts.

height 20 cm. The spheres are then allowed to deposit under the action of gravity until the desired packing is obtained. In our numerical simulations the granular bed consists of grains made from glass particles of density $\rho_g = 1520$ kg/m^3, Young's modulus $E = 6.47 \times 10^{10}$ Pa, and Poisson ratio $\nu = 0.3$. The angle of repose was kept at $\theta_r = 24^\circ$, for which the friction coefficient $\mu = 0.45$. The diameter d_g of the grains are uniformly distributed around the mean 4 mm and lies between 3.2 and 4.8 mm. The total number of grains in the bed is 123 758. After gravity deposition, the height of the granular bed is 8.5 cm and the packing fraction is 56.44%. In the experiments carried out by Jerkins *et al.* [21] for a monodispersed system the lowest packing fraction in the low pressure regime is 55%. Our simulated bed is consistent with this in the low-pressure environment. The distribution function $f(n_c)$ of coordination number n_c follows a Gaussian with mean ≈4.6 (Fig. 1).

A projectile made of the same material as the bed particles but with diameter D much larger than the mean diameter of the bed particles is incident normally at the center of the bed. For the numerical integration of the equations of motion we use the Hertz-Mindlin [22] no-slip interaction model. In this model, the interaction force between two spheres in contact is decomposed into an elastic normal force and an incremental shear force. The normal contact force f_n is given by Hertz's law, $f_n = k_n \xi_n^{3/2}$. ξ_n here is the normal overlap distance between the two spheres. The normal stiffness constant $k_n = \frac{4}{3} E\sqrt{R}$, where the equivalent radius of the two particles $R = \frac{R_1 R_2}{R_1+R_2}$ and Young's modulus $E = \frac{1}{\frac{1-\nu_1^2}{E_1}+\frac{1-\nu_2^2}{E_2}}$. In the shear direction, a linear relationship is assumed between the shear force and the tangential displacement. The tangential contact force $f_s = k_s\sqrt{\xi_n}\Delta s$. Δs is the tangential displacement increment between the two particles. The tangential contact stiffness $k_s = 2\sqrt{4R}\frac{G}{2-\nu}$. G is the average of the Shear modulus and ν is the average of the Poisson ratio of the two spheres. The maximum shear force that develops at a point in contact is determined by the Mohr-Coulomb criterion [$f_s = \min(f_s, \mu f_n)$]. In the simulations we have fixed the time step Δt at 0.6×10^{-8} s, which is much smaller than the contact time obtained from Hertzian theory for elastic contact [23]. A small damping factor of 0.01 which sets the restitution coefficient as 0.99 has also been considered. For the low-pressure conditions used here and impact velocities considered, our preliminary tests did not show any significant difference in the results for restitution values in the range 0.9 to 0.99. At this stage we use this granular bed for different impact speeds and restrict our current analyses to understanding the dynamics of the projectile as it moves through this granular bed.

To ensure our results are valid for different granular beds, we have also carried out numerical experiments on a bed with the same mean radius consisting of 119 584 particles of packing fraction 56% and average coordination number 4.3. Since both the simulations reveal the same physical behavior we choose to show the results for one of the beds.

To obtain a description of the drag forces and the dependence of the coefficients in Eq. (1) on granular beds of a range of packing fractions, extensive simulations of the behavior of the drag force acting on the impacting particle should be done on many beds with different packing fractions [24,25], polydispersities, and restitutions. Such a study is a formidable undertaking and is currently being pursued.

III. RESULTS

Our simulation results shown in Fig. 2 displays the typical dynamics observed in projectile impact studies [5]. For a range of different initial velocities, the projectile motion shows regimes characterized by large deceleration at impact, followed by slow penetration and then the final stopping inside the granular bed.

Figures 2(a) and 2(b) show respectively the time evolution of the position $z(t)$ and velocity v of the projectile inside the granular bed. The positive position and velocity values in Figs. 2(a) and 2(b) are along the downward direction inside the bed. The penetration depth increases with time until the projectile stops. The velocity shows a rapid decline initially followed by a gradual decrease. The stopping time t_{stop} also does not show any significant dependence on the initial speed. This can be observed in the inset of Fig. 2(b), where the data shows that the variations in stopping time are almost negligible at higher impact speeds ($v_0 \geqslant 2$ m/s). It should be noted that to avoid any inconsistency we have defined a threshold in the ratio v/v_0 in calculating the stopping time. In this context, see Fig. 1(b) in Ref. [2], where the authors mention that while the stopping time increases with velocity at small impact speeds, it remains almost constant for large impact speeds. In Fig. 2(b) this threshold is taken to be 10^{-3}. This behavior is also borne out in Fig. 2(c).

The motion seen in Fig. 2(c) can be *roughly* separated into three different regimes. Immediately after impact a large $\langle F_n' \rangle$ is followed by a regime in which it decays very slowly [see the inset of Fig. 2(c) for the time between 0.005 s and up to the vicinity of 0.025 s] and beyond which the force becomes very small. The boundary between the regimes is not necessarily sharp but, as we shall see, thinking of three different regimes

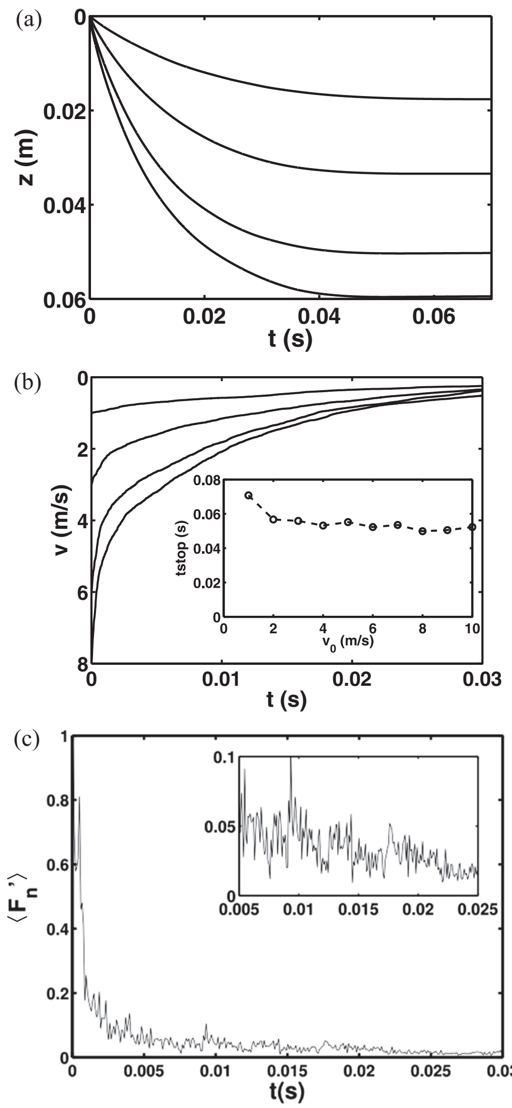

FIG. 2. Time evolution of the (a) position and (b) velocity of the projectile for different initial velocities. From top to bottom the different initial velocities are $|v_0| = 1,3,6,$ and 8 m/s, respectively. $z = 0$ is the position of the projectile when it comes in contact with the granular bed. (c) Averaged normal force acting on the projectile, normalized to its maximum value for $v_0 = 5$ m/s. Inset in (b) shows the variation of stopping time with initial speed of the projectile, while the inset in (c) shows the average normal force during the slow penetration region. Time is measured in seconds. The diameter of the projectile $D = 10d_g$. F_n' is the drag force normalized to its maximum value and $\langle \cdots \rangle$ denotes the time average, where the time averaging window used is 25 μs.

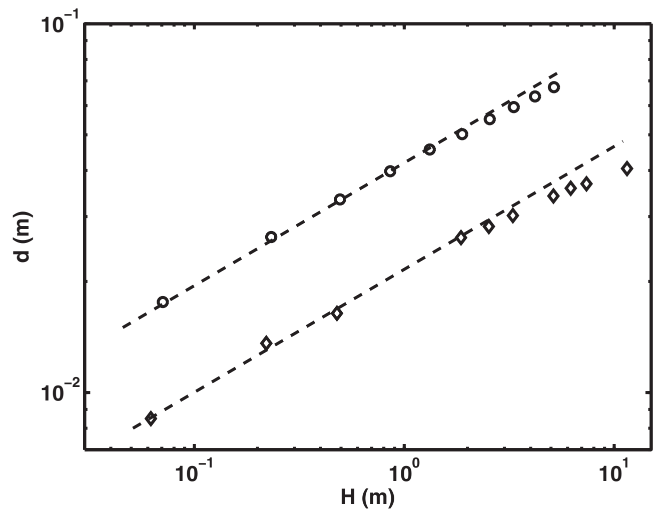

FIG. 3. Penetration depth d as a function of total falling distance for two different sphere diameter $D = 10d_g$ ($\circ$) and $D = 5d_g$ ($\diamond$), where d_g is the mean diameter of the grains. The dashed line is the 1/3 power-law fit. The points for $D = 10d_g$ are for initial velocities $v_0 = 1,2,3,4,5,6,7,8,9,$ and 10 m/s, while the initial velocities for $D = 5d_g$ are 1,2,3,6,7,8,10,11,12, and 15 m/s.

allows us to relate our observations to Eq. (1) in a natural manner.

Figure 3 shows the scaling of the penetration depth d $[d = z(t \to \infty)]$ obtained from numerical simulations as a function of the total falling distance $H = \frac{v_0^2}{2g} + d$, for projectile diameter 10 times and 5 times the mean diameter of the bed particles. The dashed line is the 1/3 power-law experimental fit [1] $[d = (0.14/\mu)(\rho_p/\rho_g)^{1/2} D^{2/3} H^{1/3}]$, ρ_p being the density of the projectile.

With increasing velocity we see departures from this scaling. This disagreement is even more pronounced for the smaller diameter projectile, for which the maximum impact velocity is 15 m/s. The maximum velocity for the larger sized projectile is 10 m/s. Since the dynamics for all the different initial conditions are the same, this deviation in penetration depth should be a natural consequence of the various pieces of the drag force that acts on the projectile.

Figures 4(a) and 4(b) provide strong indication of the validity of Eq. (1) in the low-packing-fraction regime. In Fig. 4(a) we show the variation of the average normal force $\langle F_n \rangle$ with respect to velocity. The two dashed lines fits are obtained from Eq. (1) with only the quadratic drag force but with two different coefficients of proportionality h [in this context it is important to note that there may still be some weak velocity dependence on h as borne out by Figs. 4(a) and 4(b)].

As the velocity of the projectile decreases below 2 m/s it is difficult to determine the exact nature of the drag force. To understand this we invoke the depth-dependent drag force in Eq. (1) and assume it to vary linearly with depth as $f(z) = kz$. As shown in Fig. 4(b) we indeed obtain an impressive fit for the entire range by incorporating the depth-dependent term [note that in the ordinate of Fig. 4(b) the depth-dependent drag force is reduced from the average normal force]. We can therefore imagine three different regimes in penetration based on the nature of the drag force acting on the projectile. The regimes consist of a velocity-squared dependence with different strengths in the first two regimes and both a depth and velocity dependence in the third regime. Our results are consistent with the recently reported scaling $h(z) = h \sim (\frac{m\mu}{D})(\frac{\rho_g}{\rho_p})$ and $k \sim \frac{1}{\mu}(\frac{\rho_p}{\rho_g})^{1/2}\frac{mg}{D}$ [18], and we use these in our studies. The same parameter dependence is also observed for other impact velocities but the proportionality constants are

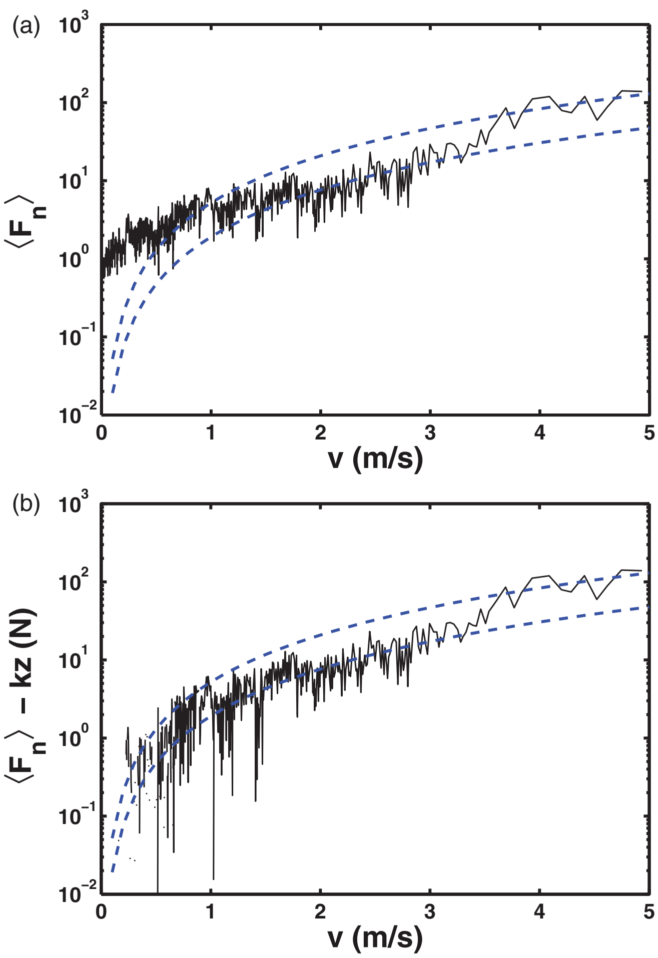

FIG. 4. (Color online) Semilog plots of (a) average normal force $\langle F_n \rangle$ and (b) the velocity-dependent part of the average normal force ($\langle F_n \rangle - kz$), acting on the projectile, plotted against velocity. The dashed lines are numerical fits corresponding to $\langle F_n \rangle \propto v^2$, with different values of the proportionality constant. The diameter of the projectile is 10 times the mean diameter of the particles in the bed.

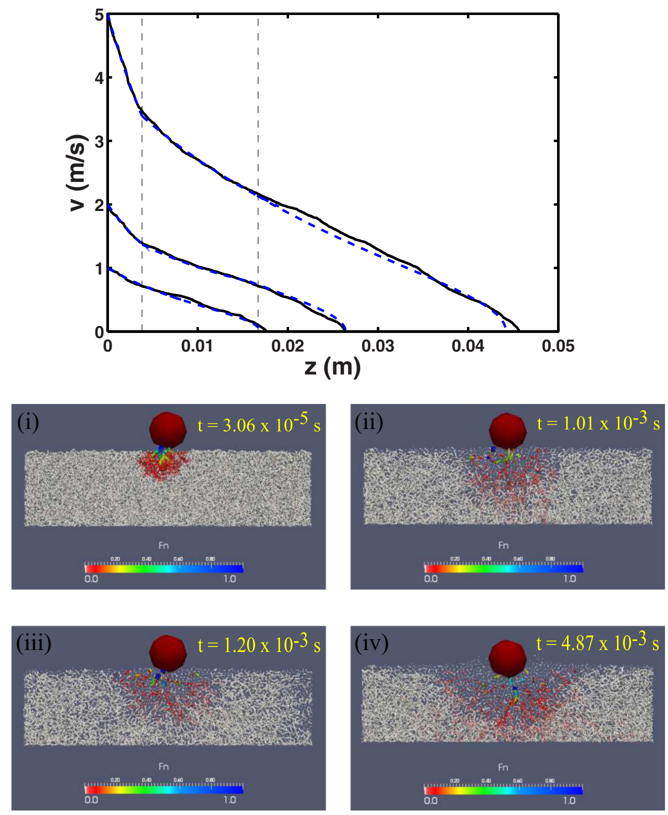

FIG. 5. (Color online) (Top) Velocity of the projectile as a function of position (solid line). The vertical dashed line is the boundary separating the different drag force experienced by the projectile. (Bottom) Cross section of the force chains at (i) 3.06×10^{-5} s, (ii) 1.01×10^{-3} s, (iii) 1.20×10^{-3} s, and (iv) 4.87×10^{-3} s. The color bar shows the normal force acting on the particles, normalized to its maximum value at each time instant. The diameter of the projectile is 10 times the mean diameter of the particles in the bed and the initial velocity is $v_0 = 5$ m/s.

seen to differ. The proportionality constants for the two dashed line fits in Fig. 4 are found to be $\simeq 9.1$ and $\simeq 3.3$, respectively.

The velocity of the projectile with depth in Fig. 5 (top) has the typical change from concave-down to concave-up as seen in the recent experiment by Katsuragi and Durian [18]. It is reassuring that our simulation clearly recovers this behavior. The vertical dashed lines approximately separate the regions with different drag forces for $v_0 \geqslant 2$ m/s, viz. a strong velocity-dependent drag force resulting in rapid decrease of velocity immediately after impact, a relatively weaker velocity-dependent drag force corresponding to the slow penetration stage, and an additional depth-dependent drag force which results in the ultimate rapid decrease of velocity to zero. Moreover, the second vertical dashed line is seen to separate the concave-down and -up trends.

The different drag regimes also correspond to different configurations of the particles in the granular bed. Figure 5 (bottom) shows snapshots of the cross section of the force chains at different times. Here Fig. 5(i) shows that immediately after impact, when the original force chains of the granular bed are still intact, the shock propagates in a hemispherical region surrounding the point of contact. At impact the projectile has to work against this force chain network and this results in the initial rapid decrease of energy. In Figs. 5(ii) and 5(iii) we see that as the projectile penetrates, the force chain beneath the projectile is broken and the bed particles in the hemispherical region are fluidized. A weaker velocity-dependent drag force acts on the projectile in this region. Finally, Fig. 5(iv) shows the force chain network once the crater opening forms. A fraction of the projectile is now surrounded by the bed particles and this is the phase in which the depth-dependent drag force becomes significant.

IV. CONCLUSIONS

In conclusion, our three-dimensional numerical simulations have shown that the temporal dynamics of the projectile is consistent with other simulations and experimental observations. With increasing impact velocity, however, the scaling of the penetration depth deviates from the one-third law. The dynamical behavior, on the other hand, is qualitatively the same for the entire velocity range and is seen to obey

Eq. (1). The coefficient of the velocity-dependent drag, $h(z)$, however, is not a constant but takes two different values. These correspond to prefluidized and fluidized force chain network of the bed as shown in Fig. 5. The behavior in Fig. 5 has also been observed recently [18], where it was also shown that Eq. (1) does not provide an accurate fit for lighter projectiles. Our present analyses concur with these observations, and the two different coefficients for the velocity-squared-dependent drag force also help explain the concave down behavior. In situations, such as heavy projectile impact, the force chains become fluidized at a much shorter time scale, and, therefore, a single value of $h(z)$ is sufficient. The depth-dependent drag force, as expected, assumes significance only at a later stage. For high impact velocity it approximately coincides with the onset of crater formation. We also expect Eq. (1) to provide a more accurate estimate for penetration depth over a wider range of impact velocities.

ACKNOWLEDGMENTS

M.T and T.R.K.M. thank ARMREB, DRDO, for a Grant-in-Aid that supported this work. In addition, T.R.K.M. also thanks CSIR for funds under a non-networked project which initiated this work. S.S. and T.R.K.M. also thank CSIR for supporting the travel of S.S. to C-MMACS for the collaborative work. S.S. thanks the Army Research Office for a STIR grant. All the authors acknowledge the contribution of the High Performance Computing (HPC) facility at C-MMACS, where the simulations were carried out.

[1] J. S. Uehara, M. A. Ambroso, R. P. Ojha, and D. J. Durian, Phys. Rev. Lett. **90**, 194301 (2003).
[2] H. Katsuragi and D. J. Durian, Nat. Phys. **3**, 420 (2007).
[3] Daniel I. Goldman and Paul Umbanhowar, Phys. Rev. E **77**, 021308 (2008).
[4] M. A. Ambroso, R. D. Kamien, and D. J. Durian, Phys. Rev. E **72**, 041305 (2005).
[5] M. P. Ciamarra, A. H. Lara, A. T. Lee, D. I. Goldman, I. Vishik, and H. L. Swinney, Phys. Rev. Lett. **92**, 194301 (2004).
[6] A. Seguin, Y. Bertho, and P. Gondret, Phys. Rev. E **78**, 010301 (2008).
[7] M. Hou, Z. Peng, R. Liu, K. Lu, and C. K. Chan, Phys. Rev. E **72**, 062301 (2005).
[8] J. R. de Bruyn and A. M. Walsh, Can. J. Phys. **82**, 439 (2004).
[9] K. A. Newhall and D. J. Durian, Phys. Rev. E **68**, 060301 (2003).
[10] S. J. de Vet and J. R. de Bruyn, Phys. Rev. E **76**, 041306 (2007).
[11] A. M. Walsh, K. E. Holloway, P. Habdas, and J. R. de Bruyn, Phys. Rev. Lett. **91**, 104301 (2003).
[12] X. J. Zheng, Z. T. Wang, and Z. G. Qiu, Eur. Phys. J. E **13**, 321 (2004).
[13] A. H. Clark, L. Kondic, and R. P. Behringer, Phys. Rev. Lett. **109**, 238302 (2012).
[14] L. Kondic, X. Fang, W. Losert, C. S. Ó'Hern, and R. P. Behringer, Phys. Rev. E **85**, 011305 (2012).
[15] M. A. Ambroso, C. R. Santore, A. R. Abate, and D. J. Durian, Phys. Rev. E **71**, 051305 (2005).
[16] A. Seguin, Y. Bertho, P. Gondret, and J. Crassous, Europhys. Lett. **88**, 44002 (2009).
[17] L. S. Tsimring and D. Volfson, Powders Grains **2**, 1215 (2005).
[18] H. Katsuragi and D. J. Durian, Phys. Rev. E **87**, 052208 (2013).
[19] T. A. Brzinski III, P. Mayor, and D. J. Durian, Phys. Rev. Lett. **111**, 168002 (2013).
[20] V. Šmilauer, E. Catalano, B. Chareyre, S. Dorofeenko, J. Duriez, A. Gladky, J. Kozicki, C. Modenese, L. Scholtès, L. Sibille, J. Stránský, and K. Thoeni, in *Yade Documentation*, edited by V. Šmilauer, The Yade Project, 1st ed. (2010); http://yade-dem.org/doc/.
[21] M. Jerkins, M. Schröter, H. L. Swinney, T. J. Senden, M. Saadatfar, and T. Aste, Phys. Rev. Lett. **101**, 018301 (2008).
[22] R. D. Mindlin, J. Appl. Mech. (ASME) **16**, 259 (1949).
[23] D. Antypov and J. A. Elliott, Europhys. Lett. **94**, 50004 (2011).
[24] P. Umbanhowar and D. I. Goldman, Phys. Rev. E **82**, 010301 (2010).
[25] N. Gravish, P. B. Umbanhowar, and D. I. Goldman, Phys. Rev. E **89**, 042202 (2014).